ATL-LARG-99-001
27 Jan 1999

Hadronic Endcap Modules Zero Pion and Electron Energy Scan Analysis from April 1998 Testbeam Data

Matt Dobbs[1], Michel Lefebvre[2], and Dugan O'Neil[3]

University of Victoria,
Victoria, Canada.

November 23, 1998

Abstract

The Hadronic Endcap modules Zero were tested in the H6 beamline at CERN in April 1998. The response and resolution are evaluated at four impact points for electrons and pions over an energy range of 20 to 180 GeV. The response varies within 1% for electrons. The electron energy resolution is parameterized as $\frac{\sigma}{E} = \frac{22.0\pm\ 0.01\%}{\sqrt{E_0}} \oplus\ 0.0 \pm\ 0.2\% \ \oplus\ \frac{0.54\pm\ 0.02}{E}$ where E_0 is expressed in GeV. The pion energy resolution (with pre-subtracted noise) is parameterized as $\frac{\sigma}{E} = \frac{78\pm\ 2\%}{\sqrt{E_0}} \oplus 5.0 \pm\ 0.3\%$.

[1]Matthew.Adam.Dobbs@Cern.CH
[2]Lefebvre@UVic.CA
[3]Dugan@UVic.CA

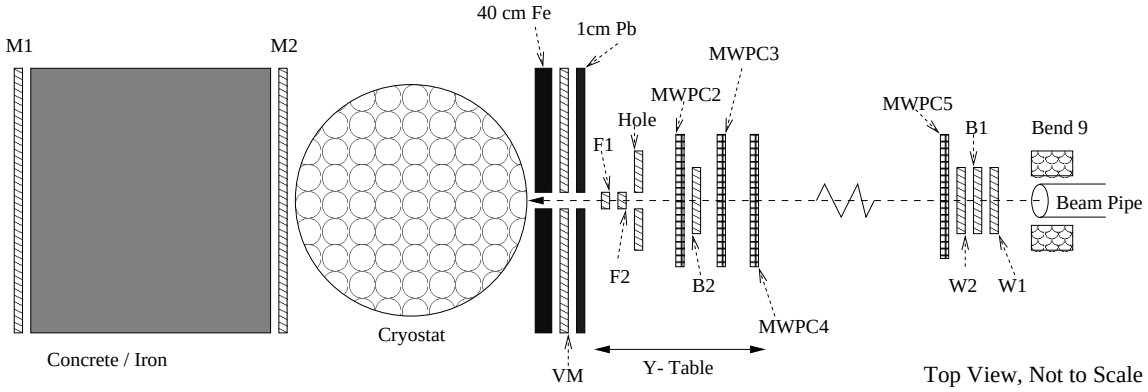

Figure 1: Setup of the HEC testbeam.

1 Introduction

The ATLAS Hadronic Endcap Calorimeter (HEC) is a liquid argon sampling calorimeter with copper absorbers [1]. Prototypes have previously been tested in beams at CERN [2]. The modules Zero are the first HEC modules built to the final ATLAS design specifications and, unlike previous prototypes, contain 10 interaction lengths effecting near full longitudinal containment of hadronic showers. Also, better lateral containment is achieved by these modules than by any previous modules.

One full ATLAS HEC will consist of 32 pie-shaped modules. The readout segmentation will be $2\pi/64$ in ϕ and 0.05-0.1 in pseudorapidity. The modules Zero consist of four phi segments (2 per module) totaling 1/16 of one endcap.

The construction of the ATLAS Hadronic Endcap modules Zero were completed in spring 1998. In April 1998, testbeam data were recorded for pion, electron and muon beams with energies ranging from 20 to 180 GeV. This paper focuses on the energy scans that were performed at several impact positions to assess the energy response and resolution of the calorimeter.

In section 2 an overview of the experimental setup is presented. The data runs are briefly described in section 3. Sections 4 and 5 concentrate on determining the response and resolution of the calorimeter to electrons and pions respectively.

2 Experimental Setup

The modules were installed in the H1 cryostat in the H6 beamline of the SPS at CERN. Trigger counters and multi-wire proportional chambers installed in the beamline (see Figure 1) provide trigger and particle identification information.

Though the Hadronic Endcap is constructed so as to provide a semi-pointing geometry in pseudorapidity, space constraints within the cryostat prevent the modules Zero from being tilted such that beam particles are incident in a pointing manner (see Figure 2). Thereby a hadronic shower will deposit energy in a larger number of cells than it would in a pointing orientation, necessitating the use of larger clusters and increasing the electronic

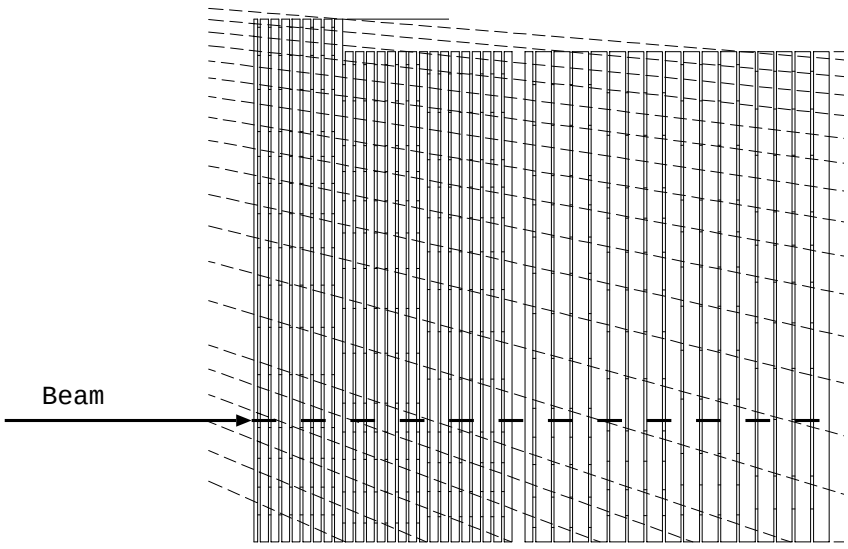

Figure 2: Orientation of the beam with respect to the calorimeter [1, Fig. 8-1]. The thick line represents the incident (non-pointing) particle beam. The thin dashed lines are drawn at constant pseudorapidity from the ATLAS interaction point, such that a particle traveling in a straight line from the vertex would follow this trajectory. The readout cells are positioned in a "semi-pointing" manner which follows these pseudorapidity lines in a stepped fashion.

noise contribution to the energy resolution.

Longitudinally the calorimeter is divided into three readout segments. The first segment ($z = 1$) consists of 8 liquid argon (LAr) gaps each separated by 2.5 cm of copper. The second segment ($z = 2$) consists of 16 LAr gaps also separated by 2.5 cm of copper. The third segment ($z = 3$) consists of 16 gaps each separated by 5 cm of copper. The change in sampling fraction in the third segment necessitates the application of a factor of two relative to the first two segments when reconstructing the energy deposited in this layer.

The two modules Zero are identical with the exception of the high resistive coating which implements the high voltage distribution within the gaps. One module uses a Carbon Loaded Paint (CLP) as a resistive coating, while the other uses a Carbon Loaded Kapton (CLK) resistive coating. In the final ATLAS design the CLK resistive coating will be employed in all modules.

Each LAr gap contains an electrostatic transformer structure which effectively divides the gap into four sub-gaps as shown in Figure 3. During the April 1998 beam period, module 2 suffered from high voltage problems in its third readout segment, requiring 1 subgap in each of the first 8 gaps to be disconnected from high voltage, while one subgap in each of the second 8 gaps had its high voltage reduced by a factor of $\frac{1}{3}$. As will be shown in the sections to follow, the resolution of module 2 is completely recoverable by using simple multiplicative depth constants to offset the effective change in sampling fraction due to HV problems.

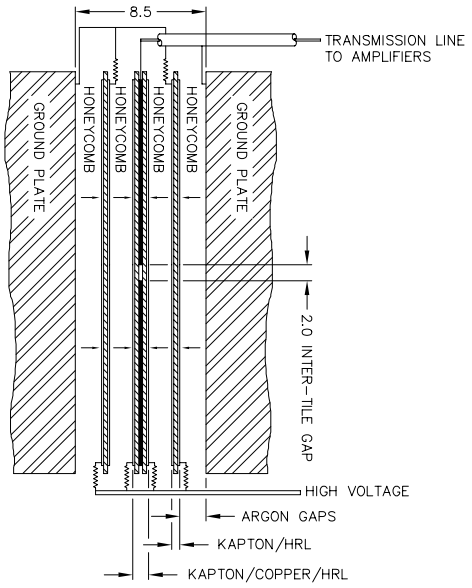

Figure 3: Subgap structure within each LAr gap [1, Fig. 8-4].

3 Data

Energy scans at 4 impact positions for electron and pion beams are analyzed. These positions are labeled D, E, H, & I, and are presented in the table below,

Position	Impact Cell	x (mm)	y (mm)
Module 1			
D	5	-100	+83
H	3	-100	-67
Module 2			
E	78	+100	+83
I	76	+100	-67

where x is measured from the center of the cryostat and y is measured from the beam's nominal impact position. Figure 4 shows the geometrical layout of the impact positions.

Impact positions D & E (H & I) belong to different modules but are identical in every other way. Positions D & E differ from positions H & I in that they each contain a tie rod which holds the layers of the calorimeter in place.

Pion data were taken at beam energies of 20, 40, 60, 80, 100, 120, and 180 GeV, while electron data were taken at 20, 40, 60, 80, 100, and 119.1 GeV. The run numbers corresponding to these data are tabulated in Appendix A.

Each run consists of 6,000 to 10,000 events (including random triggers and physics events) with the exception of the 20 GeV pion runs which suffered from low rate and contain 1000 to 2000 events.

The signal from each readout cell for each event is recorded every 25 ns for a total of 400 ns providing 16 time slices. Figure 5 shows a typical signal shape. The first 4 time slices

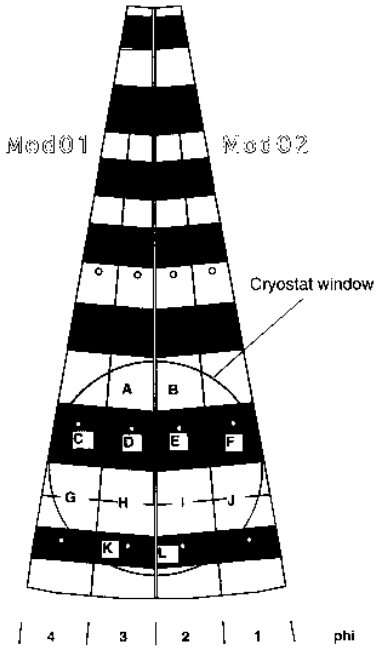

Figure 4: The geometric layout of impact positions D, E, H, & I on the front face of HEC modules Zero.

occur before the signal rise, while the signal maximum typically occurs in the 8th time slice. The energy deposited in each cell is reconstructed from the signal maximum which can be determined by a variety of methods described in section 5.1.

The pedestals for each cell are determined from the first four time slices averaged over all events within the run [4], as shown in Figure 5. On an event by event basis the average of the first 4 time slices is observed to be stable over the duration of a run.

4 Electron Energy Scans

4.1 Energy Reconstruction

The energy in each cell is reconstructed using the digital filtering method (described in Section 5.1). The electron sample is isolated by applying trigger cuts and a signal shape cut. Total electron energies are then measured by summing the energy deposited in a predefined cluster and applying a global electromagnetic scale factor, $\alpha_{\rm em}$.

[4]The use of run pedestals in lieu of event pedestals (defined as the average of the first 4 time slices for each event) provides higher statistics and hence a more precise knowledge of the pedestals for each cell. In fact, the use of event pedestals effects a considerable degradation of the calorimeter resolution.

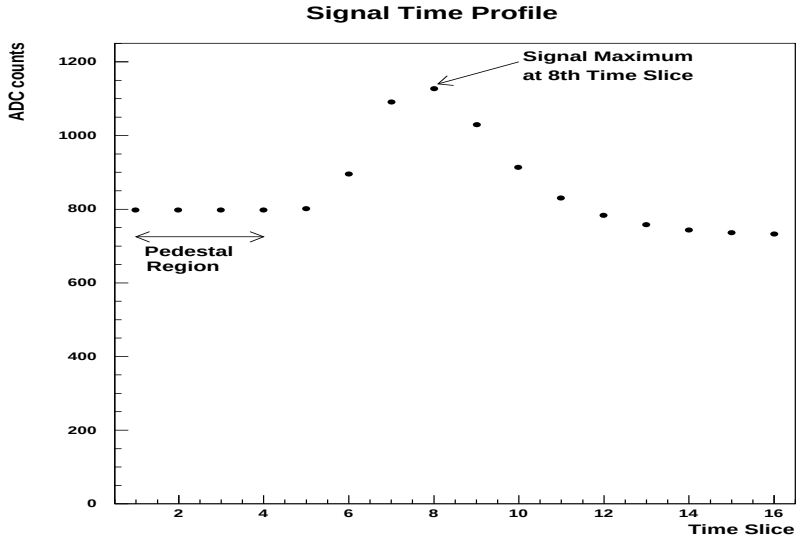

Figure 5: Sample signal time profile (average signal for run 7355, 180 GeV pions, impact position D) showing the pedestal region (time slices 1-4) and the signal maximum which typically occurs at time slice 8.

4.1.1 Trigger Cuts

Events from the electron data are selected by requiring that the following trigger logic be satisfied:

$$pretrigger \bullet \overline{halo} \bullet \overline{muon} \bullet \overline{pileup} \bullet \overline{random} \tag{1}$$

where

$$pretrigger = B1 \bullet F1 \bullet F2, \qquad halo = VM + hole, \qquad muon = M1 \bullet M2, \tag{2}$$

pileup is true when a second trigger coincides with the first, and *random* is true when the data acquisition system has requested a random trigger of any sort (hardware or software). Refer to Figure 1 for the locations of the various detectors in the testbeam setup. $B1$ is a scintillating detector upstream from the cryostat where the beam leaves the beam pipe after being bent by the last dipole magnet, Bend9. $F1$ and $F2$ are scintillating detectors which are oriented perpendicular to one another and effectively define the transverse size of the beam for triggered events. They are mounted on a motorized table (y-table) which can be displaced in the vertical direction. VM is a plane of scintillating detectors located close to the front of the cryostat with an aperture in the center coinciding with the cryostat window. *hole* is a scintillating detector mounted on the y-table with a small aperture in its center. $M1$ and $M2$ each form a plane of scintillating detectors behind the cryostat for muon identification. Čerenkov detectors are not employed to isolate electrons from pions.

4.1.2 Signal Shape Cut

The trigger cuts are not sufficient to properly veto low energy background events. A signal shape cut is used to further isolate the electron sample.

Each event is checked to ensure that at least one cell in the cluster contains a signal shape consistent with energy deposition in that cell [5]: a maximum between the seventh and ninth time slices with the signal decreasing everywhere in the vicinity of the maximum, where the vicinity is defined as the surrounding seven time slices. There are no requirements on the amplitude of this signal. Approximately 4800 - 5600 electron events satisfy the combined trigger and signal shape cuts for each data run.

4.1.3 Clustering

The energy of the incident electrons is reconstructed by summing the individual energies deposited in a cluster of 3 cells after applying hardware calibration constants. The cluster size and shape have been chosen so as to minimize the energy resolution. Figure 6 shows the clusters chosen for the 4 impact positions.

The energy deposited in each cluster is histogrammed and a Gaussian curve is fit to the data in a 2.5σ range about the mean for each run. Histograms and fits for a representative impact position (H) are shown in Figure 7.

4.1.4 Global Electromagnetic Scale, α_{em}

A single constant, α_{em}, is used to convert the energies from nA to GeV. This global electromagnetic scale is determined for each impact position by minimizing the following function:

$$\chi^2 = \sum_{\mathrm{i}}^{\mathrm{runs}} \frac{\left(\alpha_{\mathrm{em}} \left\langle E_{\mathrm{cl,i}}(\mathrm{nA}) \right\rangle - E_{0,i}\right)^2}{\sigma_i^2} \tag{3}$$

where σ_i are in GeV, $\left\langle E_{\mathrm{cl}}(\mathrm{nA}) \right\rangle$ is the mean energy arrived at by fitting Gaussian curves to the energy distributions as described in section 4.1.3, and E_0 is the nominal beam energy expressed in GeV.

The global electromagnetic scale is found to be similar at all impact points. The average over all 4 impact positions is:

$$\alpha_{\mathrm{em}} \;=\; 0.112 \text{ GeV/adc} \;=\; 3.41 \text{ GeV}/\mu\mathrm{A}. \tag{4}$$

4.2 Response

By applying α_{em} to the fit mean energy for each run, a response curve is obtained, Figure 8. The response is linear to within 1% over all impact positions. The response linearity is improved by the hardware calibration.

[5] see [3] for a description of the signal shape analysis package

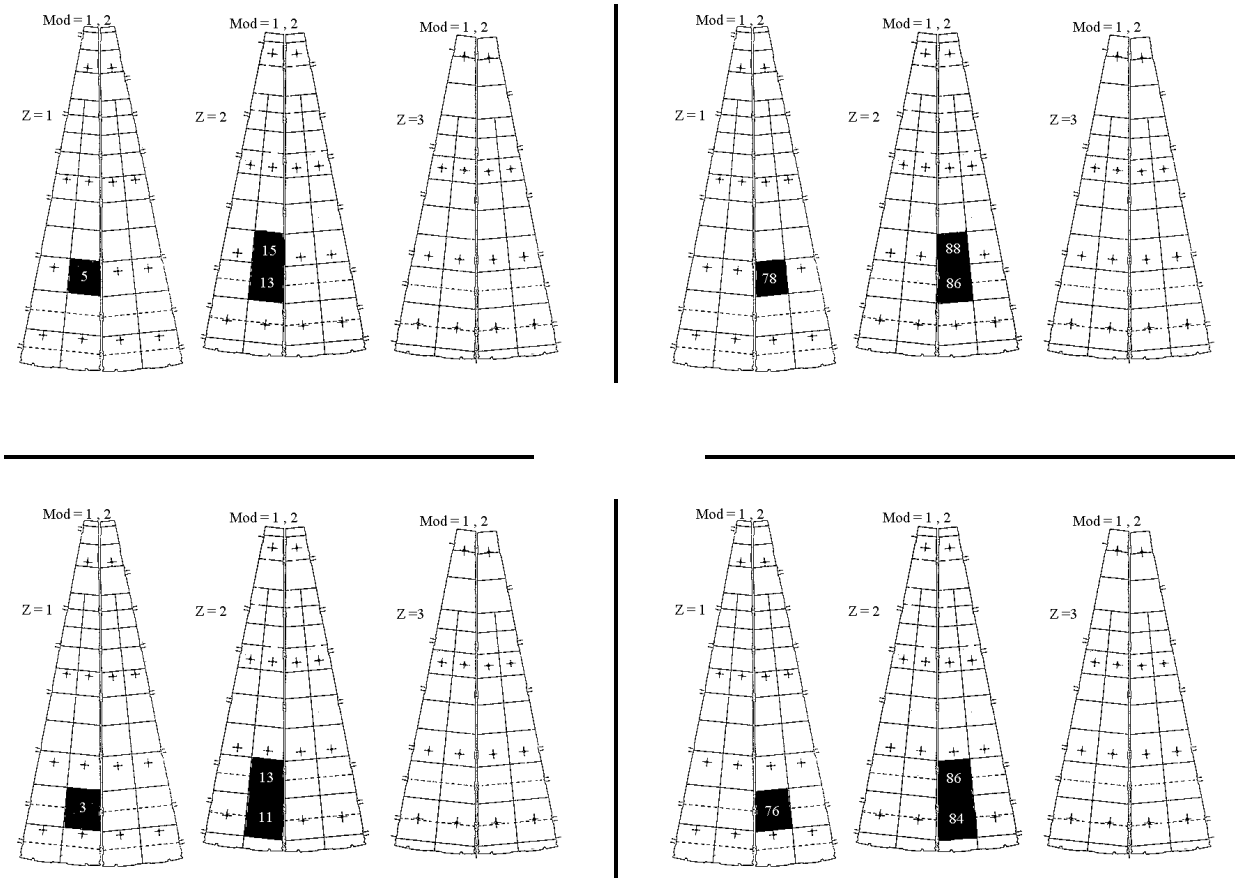

Figure 6: Map of 3 cell clusters used for electron data: impact positions D, E, I, H (clockwise from top left).

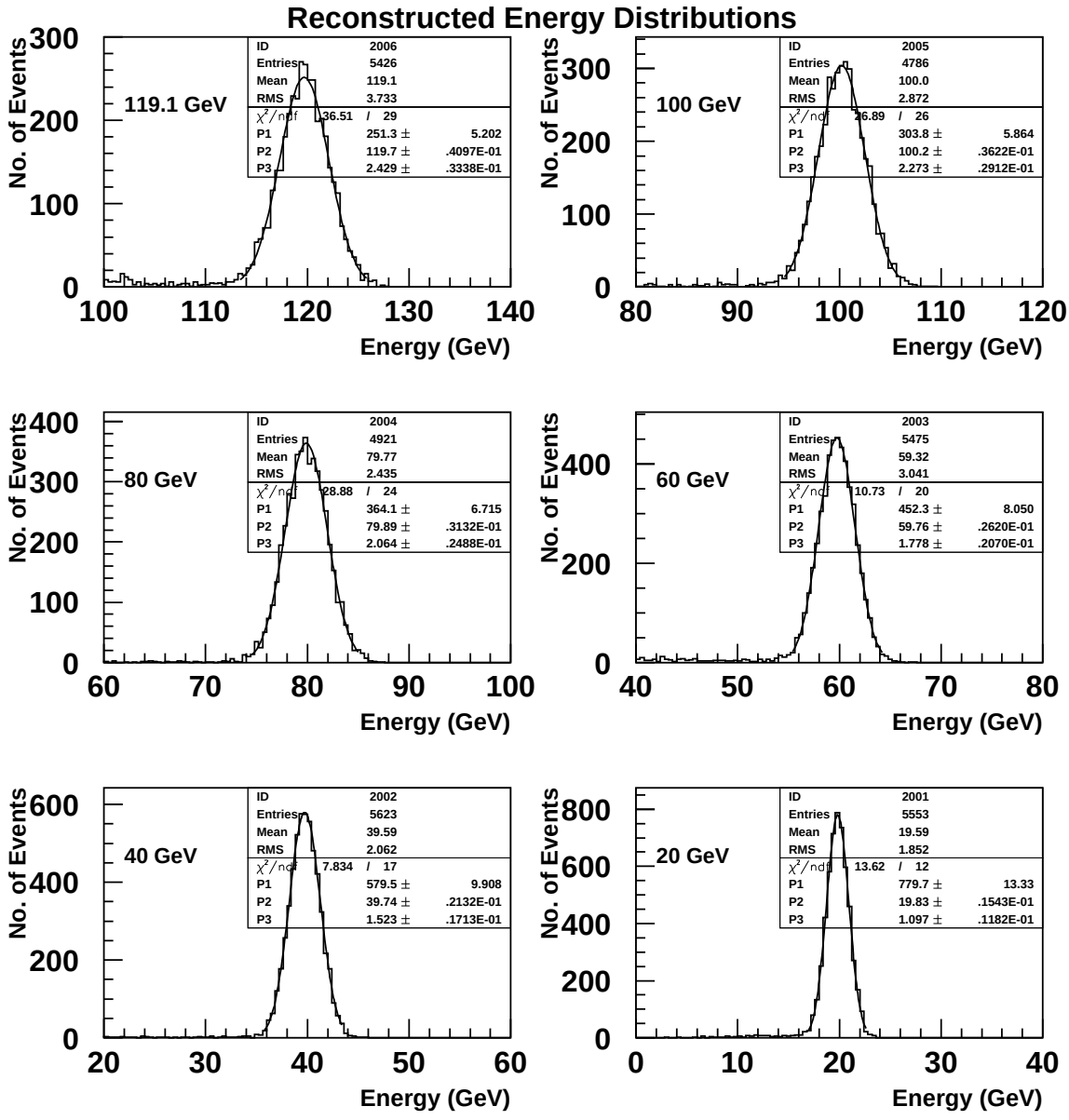

Figure 7: Electron cluster energy (calibrated data) for a typical impact point(H) for energies 119.1, 100, 80, 60, 40 and 20 GeV.

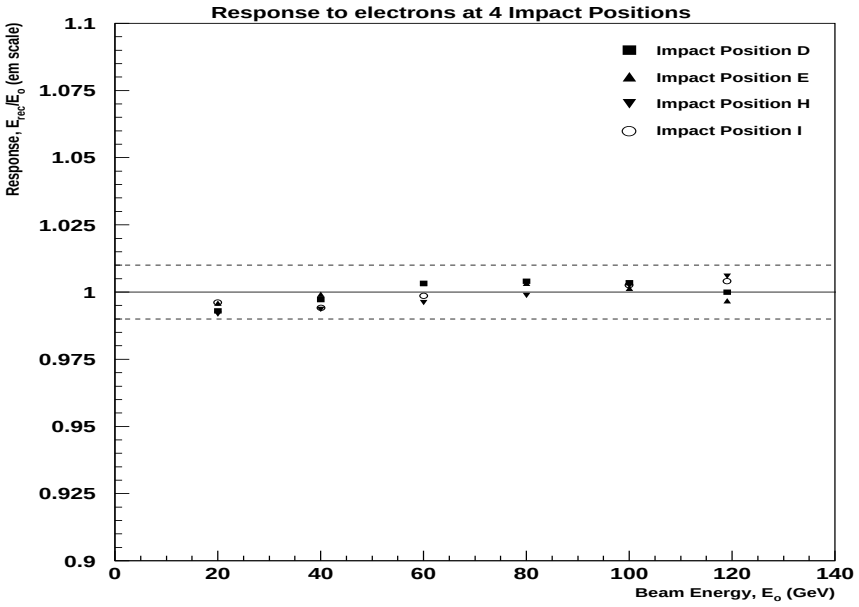

Figure 8: Electron response of calorimeter vs. beam energy.

4.3 Resolution

The energy resolution σ/E is plotted versus the beam energy in Figure 9. The resolution of the calorimeter is parameterized as:

$$\frac{\sigma}{E} = \frac{A}{\sqrt{E_0}} \oplus B \oplus \frac{C}{E}, \tag{5}$$

where A is the sampling term, B is the constant term, and C is the electronic noise term. The results of the fit for each impact position with all three parameters left free are:

Position	A(%GeV$^{\frac{1}{2}}$)	B(%)	C(GeV)	χ^2/ndf
Module 1				
D	20.6 ± 0.5	0.7 ± 0.1	0.69 ± 0.04	6.5
H	22.1 ± 0.2	0.0 ± 0.3	0.52 ± 0.04	3.0
Module 2				
E	20.0 ± 0.9	0.8 ± 0.2	0.65 ± 0.05	0.3
I	22.1 ± 0.2	0.0 ± 0.3	0.49 ± 0.04	3.0

The results are consistent over all impact positions. A combined fit produces the following result:

$$\frac{\sigma}{E} = \frac{22.0 \pm 0.01\%}{\sqrt{E_0}} \oplus 0.0 \pm 0.2\% \oplus \frac{0.54 \pm 0.02}{E}, \qquad \frac{\chi^2}{\text{ndf}} = 3.3 \tag{6}$$

where E_0 is expressed in GeV.

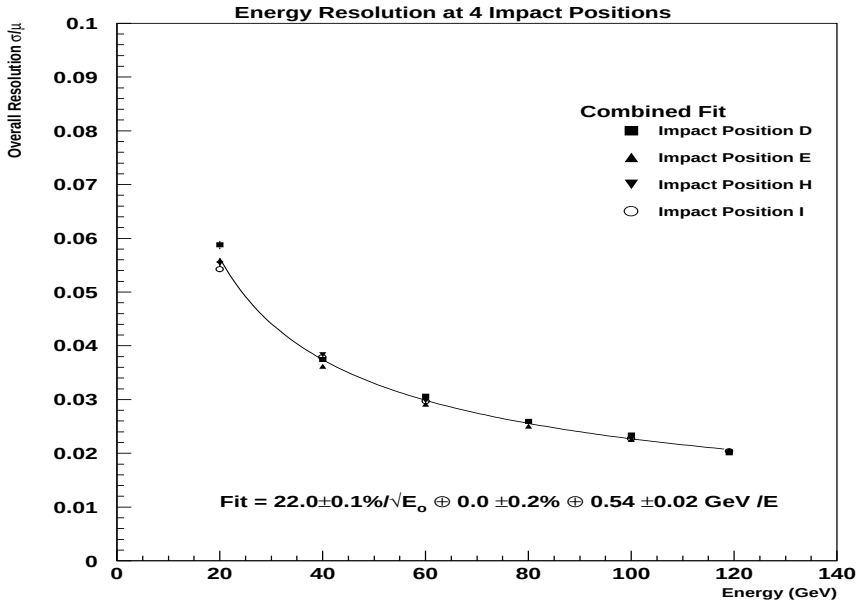

Figure 9: Electron energy resolution with 3 free parameters.

The noise term is consistent with noise measurements made from random trigger events (described in section 5.3.2).

5 Pion Energy Scans

5.1 Signal Reconstruction

Since the standard HEC testbeam readout contains 16 time slices for each channel for each event, it is necessary to define a method for reconstructing the maximum signal. Two different methods of signal reconstruction have been compared in Appendix B. The first is a simple cubic fit to 4 time slices near the maximum. This is one of the methods available in the `hec_adc` testbeam software package and is described in detail in [3]. The second method, also available in the `hec_adc` package, uses a digital filtering technique to perform the reconstruction. This technique, as explained in references [4, 5], uses the autocorrelation function of the time slices to maximize the signal/noise ratio for the determination of the time origin and amplitude of the signal. Throughout this analysis (unless stated otherwise) the digital filtering signal reconstruction method is used[6].

[6]For April 1998 data 4 cells (94,95,114,116) did not have digital filtering coefficients. Cubic fit was used for these cells.

5.2 Pion Sample

In order to remove impurities in the pion sample (eg. muons), several trigger cuts are used. These cuts have been described in detail for the electron analysis (section 4.1.4) and include a physics trigger requirement, a muon veto, and a signal shape cut. The number of pion events satisfying these cuts ranges from approximately 4000 to 9500 for the 40 to 180 GeV runs, and 350 to 450 events for the 20 GeV runs.

5.3 Evaluation of Intrinsic Calorimeter Performance

Testbeam data provides a unique opportunity to study the intrinsic performance of the hadronic endcap. To this end, a detailed analysis of pion response and energy resolution is performed herein without the use of complex optimization algorithms. Large clusters have been used to achieve near full containment. The electronic noise from these clusters is independently evaluated and subtracted to reveal the intrinsic resolution of the calorimeter.

The performance of the hadronic endcap calorimeter is evaluated using simple depth constants. These constants are not designed to optimize resolution, rather they are intended to provide a constant sampling fraction in the three readout segments of the calorimeter. This is necessary due to the increase in thickness in copper plates in the third calorimeter readout. This change in copper thickness necessitates the application of a factor of two to the readout of the rear compartment. A small modification of this scheme is introduced for module 2 in order to correct a high voltage problem in the rear of that module. Since only 3/4 of the sub-gaps were functioning in the first half of the readout segment[7] a corrective factor of 4/3 is applied to the third readout segment of this module (depth constant is 2.67 times the first two constants).

5.3.1 Energy Reconstruction

For the purpose of evaluating the intrinsic performance of the calorimeter, it is necessary to use clusters that achieve near full containment of hadronic showers. For this reason 39 cell clusters[8] are used to reconstruct pion energy. A sample cluster for impact position H is shown in Figure 10.

The signal in each cell of the cluster is summed (using the appropriate simple depth constant) to reconstruct the particle energy for each event:

$$E_{\mathrm{cl}} = \sum_{z} \left(c_z^{\mathrm{mod1}} E_{\mathrm{cl}}^{z,\ \mathrm{mod1}}(\mathrm{nA}) + c_z^{\mathrm{mod2}} E_{\mathrm{cl}}^{z,\ \mathrm{mod2}}(\mathrm{nA}) \right) \tag{7}$$

where $E_{\mathrm{cl}}^{z,\ \mathrm{mod1}}(\mathrm{nA})$ and $E_{\mathrm{cl}}^{z,\ \mathrm{mod2}}(\mathrm{nA})$ are the summed signals in readout segment z of modules 1 and 2 respectively and the simple depth constants are tabulated:

[7] The second half of the readout segment contains little energy and so is ignored in this assumption.

[8] The 39 cell clusters are chosen on a geometrical basis, though in general the chosen cells are those with the highest mean energy.

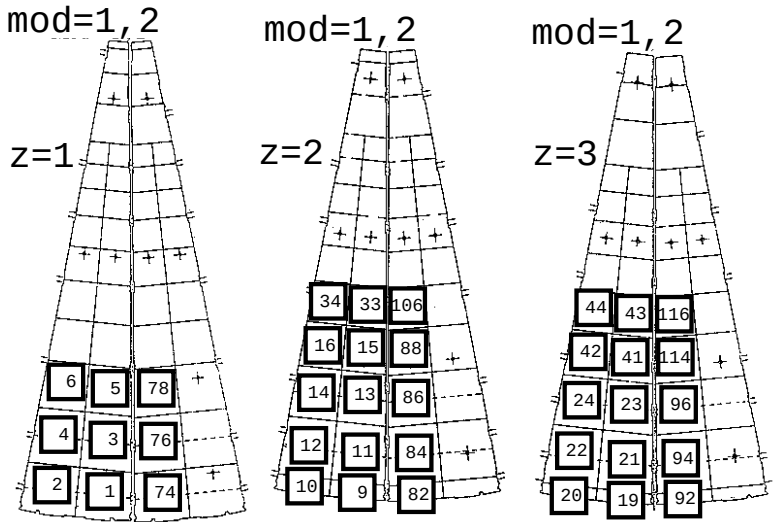

Figure 10: Map of 39 cell cluster used for pion data: impact position H.

readout segment	c_z^{mod1}	c_z^{mod2}
1	1	1
2	1	1
3	2	2.67

The hadronic scale constant (α_{had}) needed to convert E_{cl} to GeV is found using Equation 3:

$$\alpha_{\mathrm{had}} \;=\; 4.1\ \mathrm{GeV}/\mu\mathrm{A}' \tag{8}$$

where the prime is included to remind the reader that α_{had} is applied *after* the simple depth constants, and hence is not a direct conversion from nA to GeV.

The results of this energy reconstruction are shown in Figures 11 and 12. These distributions show the expected Gaussian shape.

5.3.2 Electronic Noise Evaluation

In order to evaluate the electronic noise in each cluster, the reconstructed energy of the cluster (including simple depth constants) is measured for random trigger events. The distributions obtained from this method are centered on zero and the rms deviation is used as a measurement of electronic noise. This measurement implicitly includes all correlations between individual cells. For 39 cell clusters at impact positions D, E, H and I the average noise is listed in the table below.

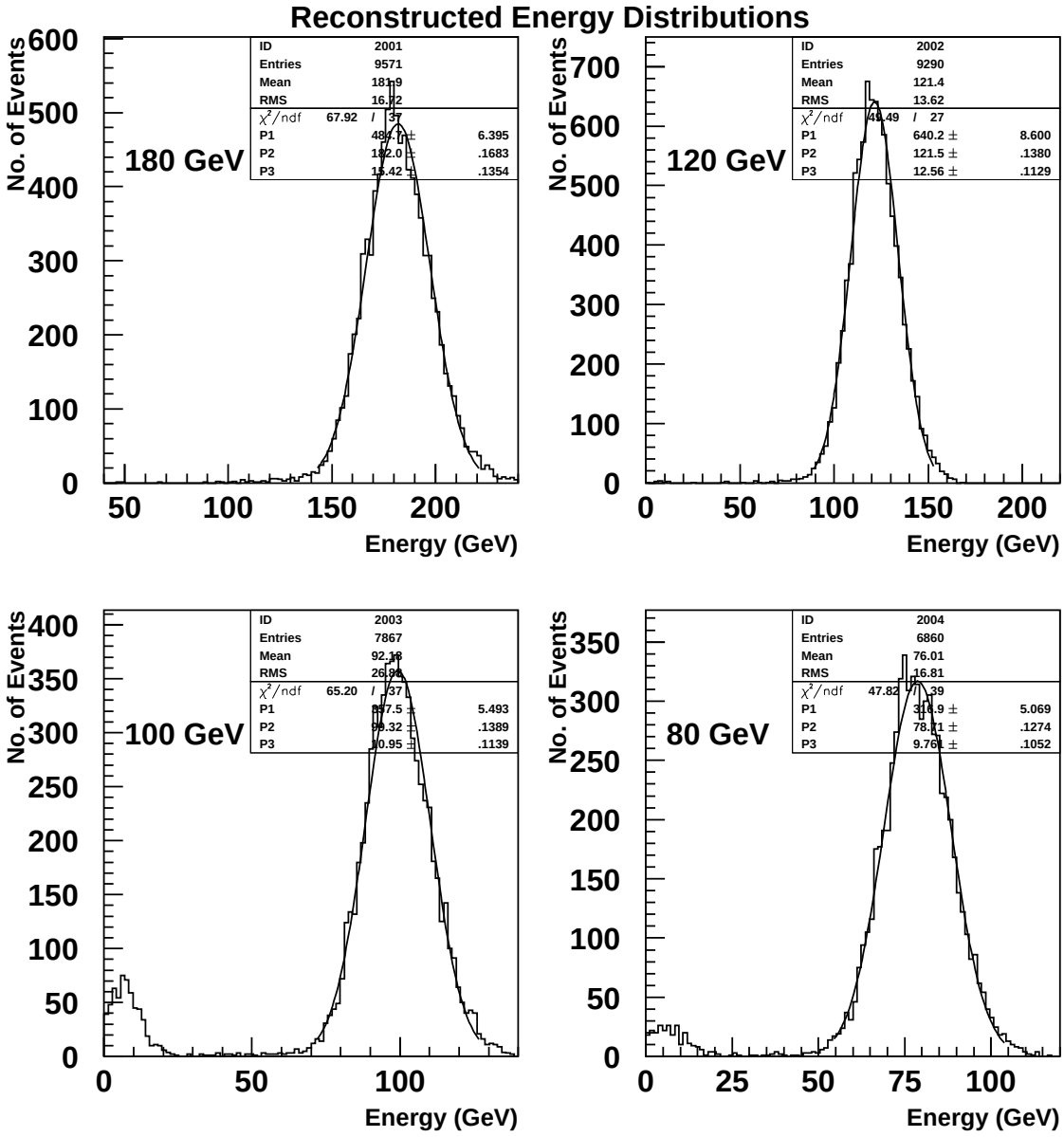

Figure 11: Pion cluster energy (calibrated data) for a typical impact point (H) after cuts and application of simple depth constants, beam energies 180 to 80 GeV. Muon contamination in the sample due to inefficiencies in the trigger and signal shape cuts can be observed at low energy, particularly for the 100 and 80 GeV runs.

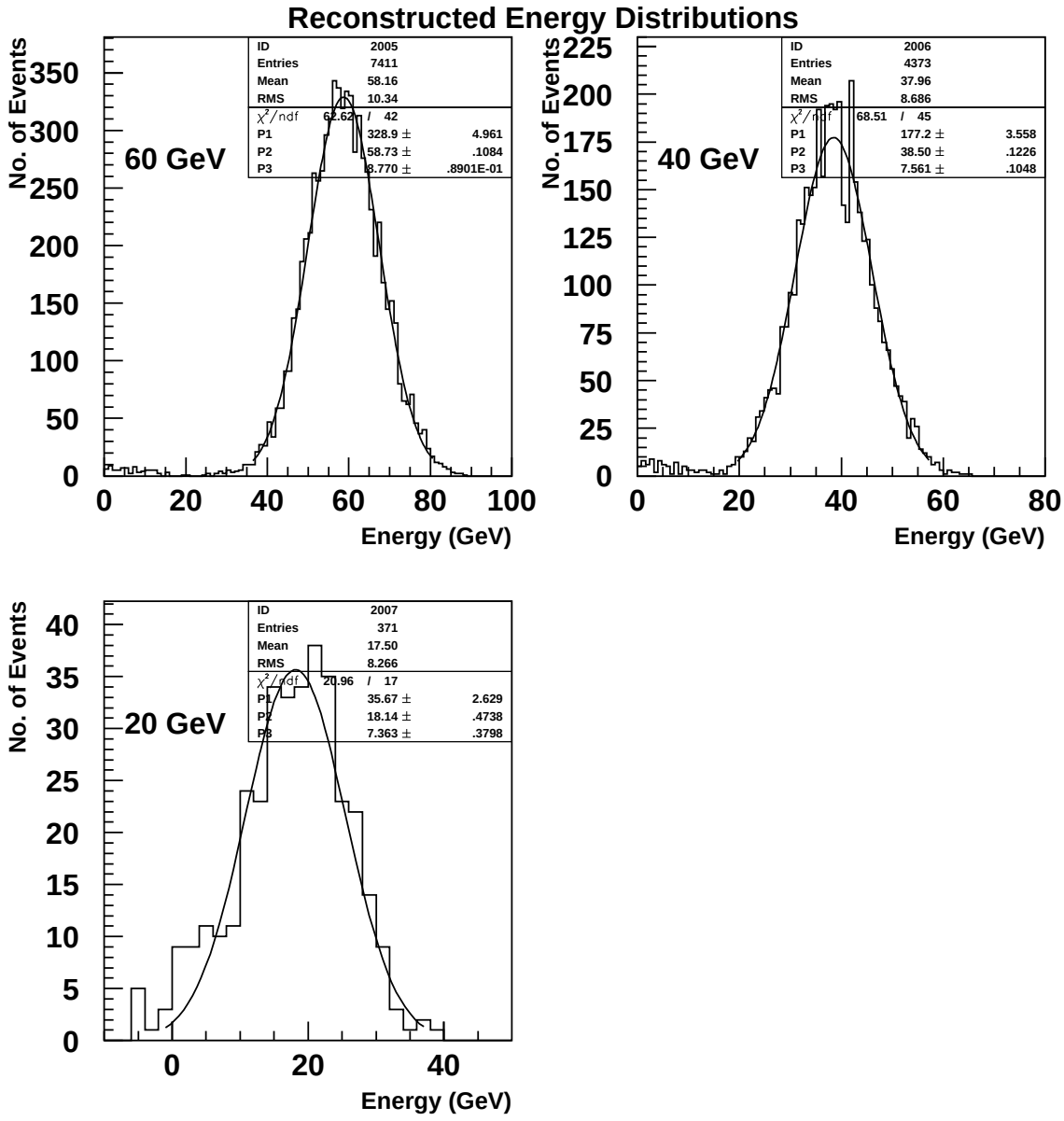

Figure 12: Pion cluster energy (calibrated data) for a typical impact point (H) after cuts and application of simple depth constants, beam energies 60 to 20 GeV.

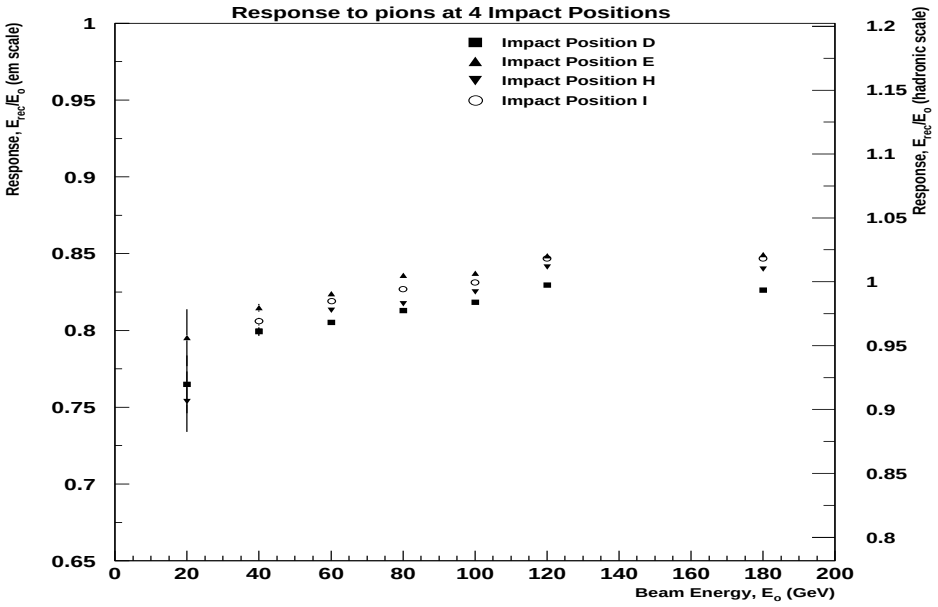

Figure 13: Pion response vs. energy is shown with two vertical scales. The scale on the left uses the electromagnetic scale constant ($\alpha_{\rm em}$ as determined from electron data) while the scale on the right uses the hadronic scale constant ($\alpha_{\rm had}$ as determined from pion data).

Impact Position	Average Electronic Noise (GeV)
D	6.38
E	5.80
H	5.69
I	5.71

5.3.3 Response to Pions

The response to pions over the energy range 20 to 180 GeV is shown in Figure 13. The left axis shows the response plotted on an electromagnetic scale ($\alpha_{\rm em}$) which contains information about the degree of non-compensation in the calorimeter (i.e. intrinsic e/h). The right axis shows the response using a global hadronic scale obtained from Equation 3. The shape of the response curve is as expected for a non-compensating calorimeter with intrinsic e/h greater than one.

5.3.4 Pion Energy Resolution

As discussed previously (Section 5.3.2), the electronic noise in a cluster of cells can be independently measured using random trigger events. Once this has been measured for a given cluster its influence can be removed and a parameterization of the intrinsic resolution

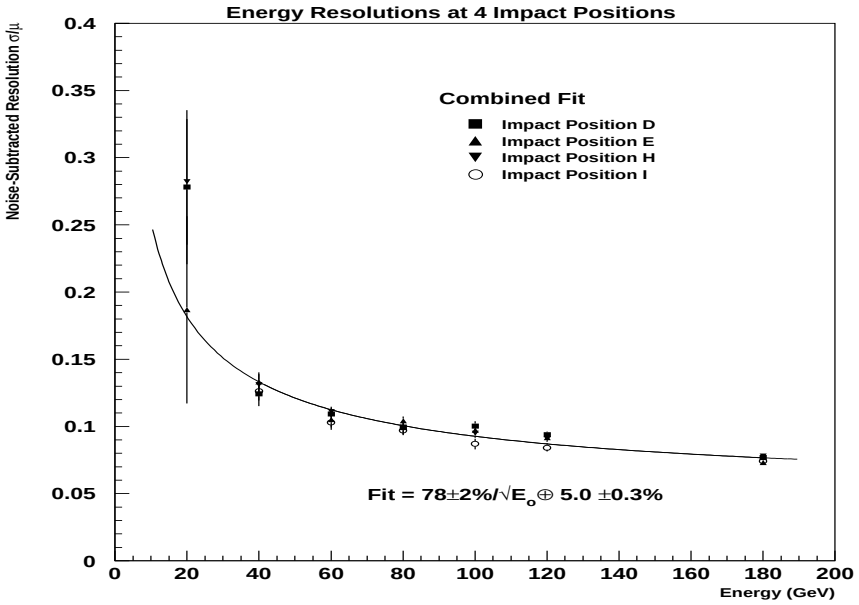

Figure 14: Intrinsic energy resolution fit over four impact positions for a 39 cell cluster and simple depth constants.

can be obtained in the form:

$$\frac{\sigma}{E} = \frac{A}{\sqrt{E_o}} \oplus B \tag{9}$$

where A and B can be interpreted as a sampling and constant term respectively.

Figure 14 shows the noise-subtracted resolution as a function of energy for 4 different impact positions for a 39 cell cluster and simple depth constants. Consistency between impact points is evident despite the high voltage problems in one of the modules. The adjustment of the simple depth constants effectively compensates for the loss of signal.

The results of fits to data for each of the four impact positions is tabulated below.

Position	A(% GeV$^{\frac{1}{2}}$)	B(%)	χ^2/ndf
Module 1			
D	77 ± 4	5.5 ± 0.5	2.5
H	84 ± 4	5.4 ± 0.4	1.3
Module 2			
E	77 ± 4	4.2 ± 0.6	2.0
I	73 ± 4	5.0 ± 0.4	1.3

A combined fit of equation 9 to the data for 4 impact positions yields the result

$$\frac{\sigma}{E} = \frac{78 \pm 2\%}{\sqrt{E_o}} \oplus 5.0 \pm 0.3\%, \qquad \frac{\chi^2}{\text{ndf}} = 1.9$$

using a 2.5σ Gaussian fit on the reconstructed energy distributions. Results for 2σ and 3σ fits have also been obtained and lead to very similar resolutions at all beam energies with sampling and constant terms consistent within error.

5.4 Optimization of Overall Resolution

5.4.1 Effect of Cluster Size on Overall Resolution

The number of cells used in a cluster influences the measured energy resolution of the calorimeter. A very small cluster may exclude a significant fraction of the pion energy, effectively creating leakage and degrading the resolution, particularly the sampling and constant terms. However, the advantage of a small cluster is that by including fewer cells the electronic noise is reduced. Also, in ATLAS small clusters may be necessary to separate jets which are close to each other. A large cluster reduces problems associated with leakage (limited by real leakage from the calorimeter) but includes many cells and hence an increased electronic noise contribution. A compromise must be made which finds the optimum overall resolution while using realistic cluster sizes.

Figure 15 shows a comparison of energy resolution for 4 different cluster sizes for position H. These clusters range from a small cluster of 10 cells to a large 39 cell cluster[9]. The results show that the best overall resolution is obtained by a cluster containing 19 cells (18 for impact position I). Clusters larger than 19 cells do not improve the energy resolution at high energies, implying that leakage from the cluster is minimal. Reducing the cluster size below 19 cells (eg. 10 cells) does not improve the resolution at low energies where the noise term takes on added significance. A sample 19 cell cluster for impact position H is presented in Figure 16.

5.4.2 Optimization of Overall Resolution Using Energy Dependent Depth Weights

The fraction of energy deposited electromagnetically (versus hadronically) varies with beam energy in a pion shower. Since the HEC is intrinsically non-compensating, the overall pion resolution can be improved by applying depth weights that vary with energy.

Energy dependent depth weights, w_z, for each impact point were obtained by minimizing the function:

$$\chi^2 \;=\; \frac{1}{\sigma^2} \sum_{\text{events}} \left(\alpha_{\text{had}} \sum_z w_z E^z_{\text{cl}'} - E_0 \right)^2 \tag{10}$$

where the outer summation is over all events that lie within 2.5σ of the Gaussian mean, the inner summation is over the three readout segments of the calorimeter, α_{had} is that found in section 5.3.4 and used for the 39 cell cluster, E_0 is the beam energy, and σ is the reconstructed width of the energy spectrum with energy dependent depth weights applied. The factor $\frac{1}{\sigma^2}$ is applied to give the function a χ^2 form. The minimization procedure produces a χ^2 per

[9]The cells chosen for a particular cluster are those which contain the highest mean energy. The clusters for various impact positions are observed to follow the same basic geometrical pattern.

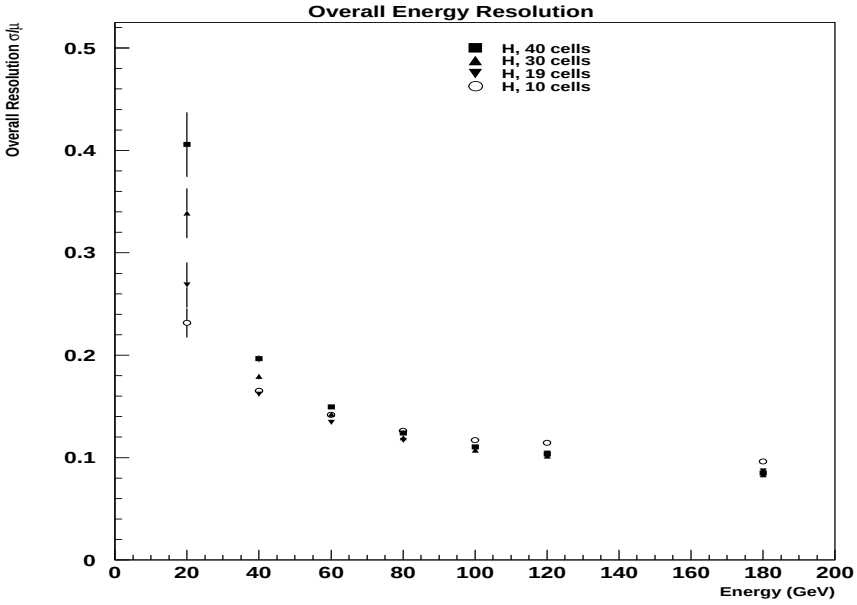

Figure 15: Comparison of overall energy resolution for four different cluster sizes for pions at position H (simple depth constants).

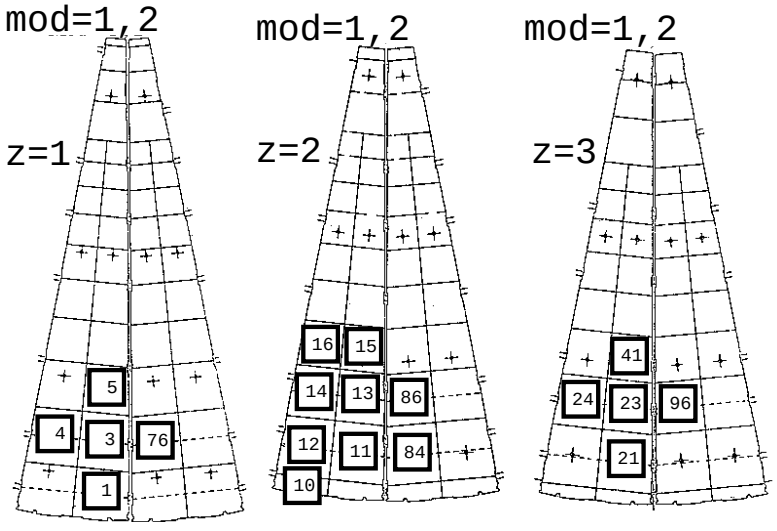

Figure 16: Map of optimized 19 cell cluster used for pion data: impact position H. The clusters for other impact positions follow the same basic pattern.

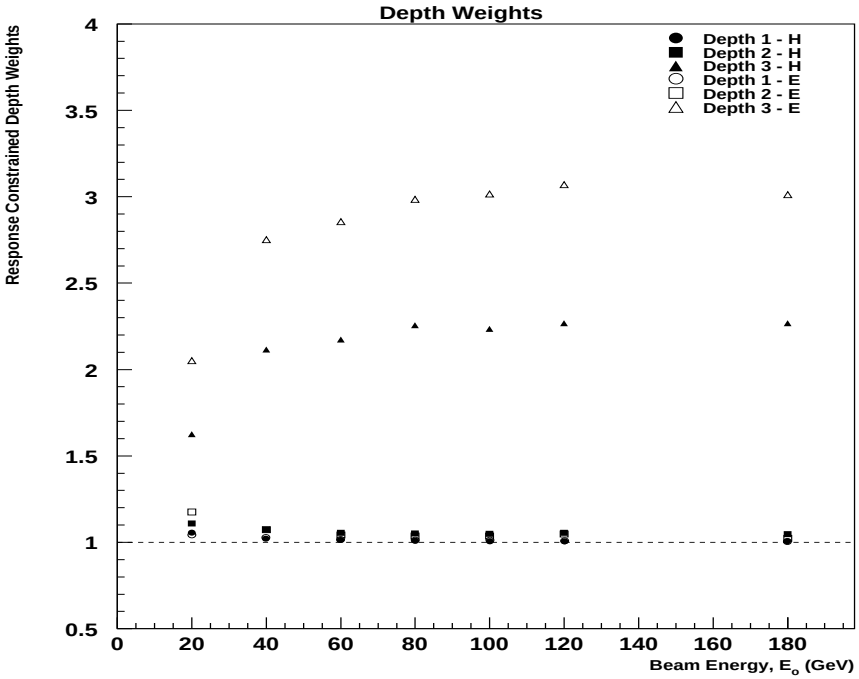

Figure 17: Effective depth weights (energy dependent depth weights multiplied by simple depth constants scaled to give uniform response) for two representative impact points. The weights presented for impact point H(E) are for module 1(2). Effect of high voltage problems in module 2 is clearly seen in the third depth weight.

degree of freedom near one for all impact points. $E^z_{\mathrm{cl}'}$ is the energy in readout segment z with simple depth constants applied, i.e.:

$$E^z_{\mathrm{cl}'} = c_z^{\mathrm{mod1}} E^{z,\ \mathrm{mod1}}_{\mathrm{cl}} + c_z^{\mathrm{mod2}} E^{z,\ \mathrm{mod2}}_{\mathrm{cl}}. \tag{11}$$

At low energies when very little signal reaches the second and third readout segments, this procedure is ineffective. Hence, this depth weighting procedure has not been employed at 20 GeV.

The energy dependent depth weights can be scaled so as to produce uniform response at all energies. This scaling does not affect the resolution curve in any way. Figure 17 shows the effective depth weights (the energy dependent depth weights multiplied by the simple depth constants, scaled to give uniform response) for a representative impact point in each of modules 1 and 2. Note that the two modules share the same energy dependent depth weight for each readout segment for each energy, but the effective depth weight for each module may differ, since the simple depth constants for the two modules are not necessarily the same (i.e. due to HV problems in the 3rd readout segment).

It should further be noted that this procedure minimizes the *overall* resolution (ie. including electronic noise). It does not serve to minimize the individual parameters of a resolution

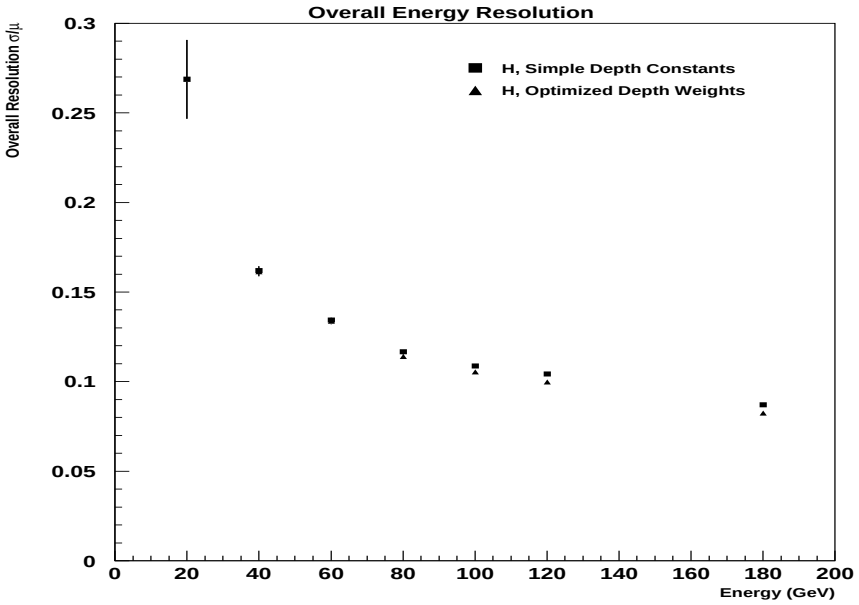

Figure 18: Overall resolution for 19 cell cluster using simple and optimized energy dependent depth weights.

parameterization such as equation 9. Thus, the overall resolution will improve with the application of energy dependent depth weights, but a parameter such as the sampling term *will not necessarily improve.*

The energy dependent depth weights can be used to check the validity of the simple depth constants. If these constants are inaccurate, the minimization procedure would produce energy dependent depth weights which shift the effective depth weights significantly away from the original depth constants at all energies. Factors of 1 are preferred for the first readout segments of both modules, while a factor of 2 is preferred for the 3rd readout segment of module 1 and a factor of roughly 2.67 is preferred for the 3rd readout segment of module 2 (affected by HV problems). The effective depth weights follow the expected behavior, justifying the naive assumptions used to calculate the simple depth constants.

The overall resolution is evaluated using the optimized energy dependent depth weights and the optimized 19 cell cluster and is presented in Figure 18. A plot of the overall resolution using simple depth constants is superimposed. The use of optimized energy dependent depth weights produces a noticeable improvement in overall resolution at higher energies.

6 Conclusions

The Hadronic Endcap modules Zero were successfully tested in April 1998.

The use of digital filtering for signal reconstruction effects an improvement in response

and resolution over a simple cubic fit.

Using a 3 cell cluster, the response to electrons is found to be constant to within 1%. A combined fit over all impact positions produces the following parameterization for the energy resolution (E_o in GeV):

$$\frac{\sigma}{E} = \frac{22.0 \pm 0.1\%}{\sqrt{E_o}} \oplus 0.0 \pm 0.2\% \oplus \frac{0.54 \pm 0.02}{E}.$$

Large clusters and simple depth constants are used to extract intrinsic calorimeter parameters from pion data. The intrinsic response to pions follows the expected behaviour for a non-compensating calorimeter with e/h greater than one. The intrinsic energy resolution can be parameterized as

$$\frac{\sigma}{E} = \frac{78 \pm 2\%}{\sqrt{E_o}} \oplus 5.0 \pm 0.3\%$$

from a combined fit over data from four impact positions. The performance at all four impact positions studied are comparable after the application of simple depth constants to compensate for high voltage problems in module 2. These constants are reproducible using energy dependent depth weights optimized with the procedure outlined in section 5.4.2.

A 19 cell cluster is the optimum cluster size for reconstructing the pion energy when electronic noise is not pre-subtracted (i.e. best overall resolution). The use of optimal energy dependent depth weights improves the overall resolution.

7 Acknowledgments

The authors would like to thank Andrei Minaenko, Peter Schacht and Hasko Stenzel for many useful discussions.

References

[1] ATLAS Collaboration, *ATLAS Liquid Argon Technical Design Report*, December 15, 1996.

[2] ATLAS - HEC Collaboration, "Electron and Pion Test Beam Data Analysis of the Hadronic Endcap Prototype Calorimeter", *ATLAS Liquid Argon Note No. 95*, April 16, 1998.

[3] Lefebvre, M. and O'Neil, D., "The HEC Testbeam Offline Software: The hec_adc Package", *ATLAS LAr Note - in progress*. Refer to `http://wwwhep.phys.uvic.ca/~uvatlas/hec_adc/hec_adc.html`.

[4] Cleland, W.E. and Stern, E.G., "Signal processing considerations for liquid ionization calorimeters in a high rate environment", *Nuclear Instruments and Methods in Physics Research*, A 338(1994) 467-497.

[5] Kurchaninov, L., Levitsky, M., "Optimal Weighting of signal Samples for LAr Calorimeters", *ATLAS Liquid Argon Note No. 44*, July 14, 1996.

[6] Groom, Don, "What really goes on in a hadron calorimeter?", presented at *VII International Conference on Calorimetry in High Energy Physics* at the University of Arizona, Tucson, Arizona, November 9-14, 1997. Refer to `http://pdg.lbl.gov/~deg/calor97.html`.

A Data Samples

The run numbers for the data used in this analysis are tabulated below.

Electron Data				
Energy (GeV)	point D Run #	point E Run #	point H Run #	point I Run #
20	7353	7350	7352	7351
40	7298	7291	7295	7294
60	7255	7259	7253	7260
80	7299	7311	7303	
100	7334	7341	7330	7342
119.1	7065	7088	7071	7079
Pion Data				
Energy (GeV)	point D Run #	point E Run #	point H Run #	point I Run #
20	7354	7371	7369	
40	7297	7292	7296	7293
60	7281	7287	7280	7285
80	7300	7312	7304	7310
100	7335	7340	7331	7343
120	7196	7154	7182	7146
180	7355	7359	7356	7360

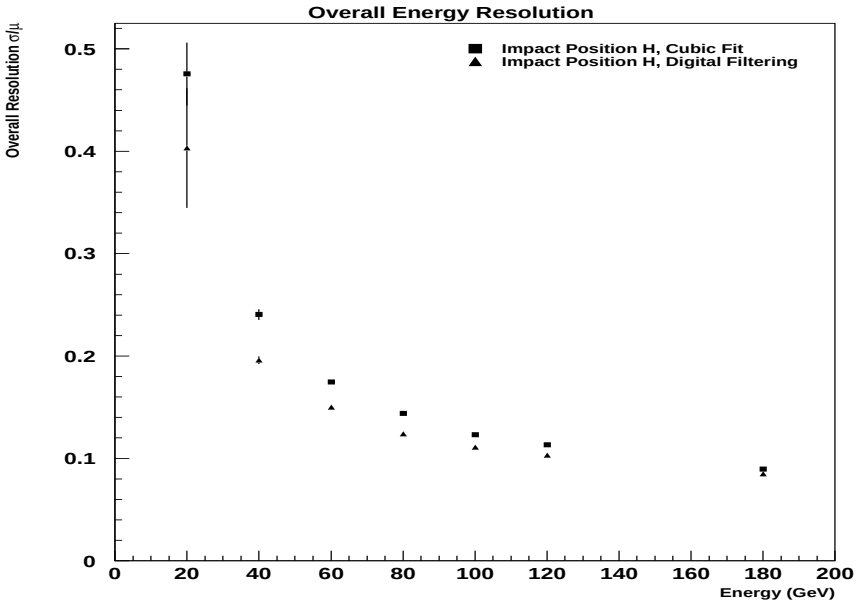

Figure 19: Comparison of cubic fit and digital filtering resolution for pions.

B Comparison of Signal Reconstruction Methods

As described in section 5.1, there are several different ways to reconstruct the signal amplitude in each cell. For all impact positions two methods have been compared in detail: cubic fit and digital filtering.

The effect of the different signal reconstruction methods on energy resolution has been evaluated. Figure 19 shows a comparison of the resolution for both methods for impact position H (39 cell clusters, simple depth constants). The resolution from cubic fit is worse than that from digital filtering at all energies. The effect is more pronounced at low energies where electronic noise makes a large contribution to the overall resolution. This effect is expected because the digital filtering method is designed to reduce noise. Also, the cubic fit method tends to overestimate the energy in cells with low signals and thus, when the signal in a particular cell is low, a systematic high-energy bias is produced. When the cubic fit is used to reconstruct zero energy signals from random trigger events it will measure above zero average energies in each cell, a clear indication of this bias. This version of the cubic fit algorithm uses a special treatment of low-signal cells in an attempt to address this problem. If the signal falls below 10 times the pedestal rms of the cell, the 8th time slice is used instead of a cubic fit to four time slices. This helps to reduce the bias, but still leads to worse resolution than digital filtering at low energies. Due to these effects, digital filtering has been chosen as the preferred signal reconstruction method for this analysis.